UC Irvine
UC Irvine Previously Published Works

Title

Ionic-resolution protoacoustic microscopy: A feasibility study

Permalink

https://escholarship.org/uc/item/2rz826bn

Journal

Applied Physics Letters, 124(5)

ISSN

0003-6951

Authors

Pandey, Prabodh Kumar
Gonzalez, Gilberto
Cheong, Frederick
et al.

Publication Date

2024-01-29

DOI

10.1063/5.0188650

Peer reviewed

Ionic-resolution protoacoustic microscopy: A feasibility study ⊘

Prabodh Kumar Pandey ⓘ ; Gilberto Gonzalez ⓘ ; Frederick Cheong ⓘ ; Ce-Belle Chen ⓘ ;
Andrew A. Bettiol ⓘ ; Yong Chen; Liangzhong Xiang ✉ ⓘ

Check for updates

View Online   Export Citation   CrossMark

13 February 2024 22:05:43

Journal of Applied Physics

Special Topic: Phase-change Materials and Their Applications

Submit Today

AIP Publishing

Ionic-resolution protoacoustic microscopy: A feasibility study

View Online   Export Citation   CrossMark

Prabodh Kumar Pandey,[1] (iD) Gilberto Gonzalez,[2] (iD) Frederick Cheong,[3] (iD) Ce-Belle Chen,[3] (iD) Andrew A. Bettiol,[3] (iD)
Yong Chen,[2] and Liangzhong Xiang[1,4,5,a)] (iD)

AFFILIATIONS

[1]Department of Radiological Sciences, University of California, Irvine, California 92697, USA
[2]Department of Radiation Oncology, University of Oklahoma Health Sciences Center, Oklahoma City, Oklahoma 73104, USA
[3]Centre for Ion Beam Applications, Department of Physics, National University of Singapore, 2 Science Drive 3, Singapore 117542, Singapore
[4]Department of Biomedical Engineering, University of California, Irvine, California 92697, USA
[5]Beckman Laser Institute, University of California, Irvine, California 92612, USA

[a)]Author to whom correspondence should be addressed: liangzhx@hs.uci.edu

ABSTRACT

Visualizing micro- and nano-scale biological entities requires high-resolution imaging and is conventionally achieved via optical microscopic techniques. Optical diffraction limits their resolution to ∼200 nm. This limit can be overcome by using ions with ∼1 MeV energy. Such ions penetrate through several micrometers in tissues, and their much shorter de Broglie wavelengths indicate that these ion beams can be focused to much shorter scales and hence can potentially facilitate higher resolution as compared to the optical techniques. Proton microscopy with ∼1 MeV protons has been shown to have reasonable inherent contrast between sub-cellular organelles. However, being a transmission-based modality, it is unsuitable for *in vivo* studies and cannot facilitate three-dimensional imaging from a single raster scan. Here, we propose proton-induced acoustic microscopy (PrAM), a technique based on pulsed proton irradiation and proton-induced acoustic signal collection. This technique is capable of label-free, super-resolution, 3D imaging with a single raster scan. Converting radiation energy into ultrasound enables PrAM with reflection mode detection, making it suitable for *in vivo* imaging and probing deeper than proton scanning transmission ion microscopy (STIM). Using a proton STIM image of HeLa cells, a coupled Monte Carlo+k-wave simulations-based feasibility study has been performed to demonstrate the capabilities of PrAM. We demonstrate that sub-50 nm lateral (depending upon the beam size and energy) and sub-micron axial resolution (based on acoustic detection bandwidth and proton beam pulse width) can be obtained using the proposed modality. By enabling visualization of biological phenomena at cellular and subcellular levels, this high-resolution microscopic technique enhances understanding of intricate cellular processes.

Published under an exclusive license by AIP Publishing. https://doi.org/10.1063/5.0188650

Microscopy has revolutionized our understanding of cellular biology by granting us an unprecedented window into the intricate world of cells. This powerful technique facilitates a magnified view of cellular structures, enabling scientists to observe and analyze their morphology, behavior, and interactions with exceptional clarity, offering insights that have paved the way for medical advancements and a deeper understanding of life itself.

Traditional optical microscopic modalities are known to have diffraction-limited spatial resolution.[1] The diffraction limit in microscopy represents a fundamental constraint on the ability to resolve fine details in an optical imaging system and is determined by the wavelength of light being used and the numerical aperture of the optical system. When attempting to image structures smaller than the diffraction limit, light waves tend to interfere and create blurred images.

Techniques that overcome this limitation are classified as super-resolution microscopy. Among the optical super-resolution techniques, structured illumination microscopy (SIM)[2] is known to have ∼100 nm lateral and ∼300 nm axial resolution limit, because of the diffraction-limited structural illumination.[3] Other modalities, such as stimulated emission depletion (STED), photo-activated localization microscopy (PALM), and stochastic optical reconstruction microscopy (STORM), have been reported to demonstrate sub-100 nm resolution. However, each of these techniques requires rigorous evaluation of fluorescent probes prior to their practical application, which presents a

13 February 2024 22:05:43

notable challenge.[4] Several researchers have in the past performed multi-physics simulations by combining light transport, heat propagation, and acoustic propagation models to assess the imaging abilities of photoacoustic and optical imaging modalities.[5–11] In comparison with the UV-Vis and NIR photons, x-rays have shorter wavelengths ($\sim$nm) and, hence, when employed for microscopy, can yield sub-100 nm spatial resolution. However, lens-based x-ray microscopic systems are constrained by resolution limits imposed by the lenses and efficiency losses,[12] while x-ray diffraction microscopes grapple with the significant challenge of radiation-induced damage.[13]

Electron-based microscopic techniques, such as scanning electron microscopy (SEM)[14] and transmission electron microscopy (TEM),[15] are established microscopic modalities, which are known to yield $\sim$10–100 nm spatial resolution for surface/topographic studies and thin samples. High large-angle scattering of electrons limits their application for thick biological samples.[16] Moreover, for volumetric (3D) microscopy, these techniques require fine sectioning of the sample with each slice scanned/imaged and then concatenated for 3D rendering. Therefore, volumetric 3D microscopy using TEM/STEM comes at a higher cost (microtomes/ultra-microtomes) and longer imaging times.[17]

Protons (with kinetic energy $\sim$1–5 MeV; hereafter referred to as MeV protons) can preserve their paths as they traverse dense biological specimens of $\sim$2–10 μm thickness. Their trajectories predominantly hinge on their interactions with both atomic electrons (electrons bound to the atomic nuclei) and nuclei within the material. Notably, MeV protons primarily engage with atomic electrons in the target, and owing to the substantial disparity in momentum between MeV protons and atomic electrons, the primary ion scattering effect remains minimal. Consequently, the paths of MeV protons experience only minor deviations as they traverse the sample. Moreover, MeV protons have de Broglie wavelengths of the order of $\sim$10 fm, and hence can in principle be focused to much shorter scales (experimentally $\sim$20 nm achieved[18]) and potentially facilitate higher resolution as compared to the optical imaging techniques. Protons' energy deposition in cells depends upon the local electron density, which is known to vary significantly among various intracellular organelles depending upon their chemical composition.[19] At lower kinetic energies ($\sim$a few MeVs), protons are known to have demonstrated reasonable electron density-based contrast between cellular and intracellular entities.[20]

Scanning transmission ion microscopy (STIM)[20,21] and microscopy based on ion-beam (proton or helium-ion) induced fluorescence[18,20] utilize these advantages to achieve super-resolution (sub-50 nm) imaging capabilities. Being a proton transmission-based modality, STIM requires protons to traverse through the sample and reach the detector with minimal directional deviation [Fig. 1(a)]. This limits the applicability of STIM for thick samples as well as *in vivo* imaging. Moreover, obtaining three-dimensional STIM imaging involves rotating the biological cell to gather a series of energy loss projection data, followed by a subsequent process of 3D image reconstruction, thus making the volumetric STIM tedious.[22] In this paper, through coupled proton transport and acoustic wave propagation-based computational studies, we demonstrate the feasibility of proton-induced acoustic microscopy [or protoacoustic microscopy (PrAM)] that is capable of super-resolution three-dimensional imaging of cells, possibly live cells as well. PrAM is based on pulsed proton beam irradiation and subsequent detection of time-domain proton-induced

acoustic (hereafter referred to as protoacoustic) signals. Being a proton absorption and acoustic detection-based modality, PrAM can facilitate both transmission and reflection mode detection and deeper imaging as compared to STIM, as shown in Fig. 1(b). Moreover, protoacoustic waves are generated at the site of proton energy deposition. The time-of-flight of these waves is used to determine the depth of the cellular structures. This depth-resolved information enables the reconstruction of 3D images from a single raster scan.

The energy deposited by a proton beam along the path can be expressed as[23]

$$\mathrm{E}(\vec{r}) = \Phi(\vec{r})\mathrm{S}(\vec{r}), \qquad (1)$$

a product of the local proton fluence (Φ) and the stopping power (S), which is defined as the decrease in the kinetic energy of the protons while traveling a unit distance (commonly termed as $-\frac{dE}{dx}$). Here, we consider the beam traveling along the z direction, representing the proton kinetic energy by T. Therefore, in this paper, we express S as $-\frac{dT}{dz}$. For protons with speed v ($= \beta c$) and kinetic energy T, traveling a distance z into a medium with mean excitation energy I, the stopping power can be expressed as per Bethe's formula,[24]

$$\mathrm{S}(\vec{r}) = -\frac{dT}{dz} = \frac{4\pi \mathrm{n}(\vec{r})}{m_e c^2 \beta^2}\left(\frac{e^2}{4\pi\epsilon_0}\right)^2 \ln\left(\frac{2\mathrm{m_e}c^2\beta^2}{\mathrm{I}\left(1-\beta^2\right)} - \beta^2\right) \qquad (2)$$

with m_e being the mass of an electron, c being the speed of light in vacuum, ϵ_0 being the electric permittivity in vacuum, and $n(\vec{r})$ being the local electron density in the region. As the protons enter the material, they typically undergo multiple small-angle Coulomb scattering interactions and lose very little kinetic energy initially. This is because at the beginning of their path, they have relatively high β and interact only weakly with electrons and nuclei in the material. As they penetrate deeper, the protons slow down and the stopping power increases. The axial fluence at a distance z from the center of a circular beam (radius: r_0) will have contribution from the in-scattering of the pencil beams, and with the protons penetrating deeper, it decreases as

$$\Phi(x \to 0, y \to 0, z) \sim \Phi(\vec{0})\left(1 - e^{-r_0^2/\sigma(z)^2}\right), \qquad (3)$$

where $\sigma(z)$ is the radial standard deviation characterizing the broadening of an infinitesimally thin pencil beam at depth z in the medium.[25] The radial broadening of the beam inherently depends on the composition of the medium and the kinetic energy of the incident protons. From Eqs. (1)–(3), we conclude that the energy deposited by protons in the target implicitly relates to its chemical composition. As per Eq. (1), the axial energy deposition is a product of the stopping power [Eq. (2)] and the axial fluence [Eq. (3)].

For therapeutic proton beams, the stopping power term dominates the axial fluence term, thus giving rise to the Bragg peak region, where the energy deposition by a therapeutic proton beam is known to be predominantly concentrated. This makes protons a lucrative option for radiation therapy for treating tumors.[26,27] For thin proton beams [$r_0 \ll \sigma(z = R)$, R being the proton range], the fluence term dominates the stopping power term and the energy deposition along the central axis decreases with depth due to out-scattering of protons, thus vanishing the Bragg peak. For a broader beam, however, the axial energy deposition is restored due to in-scattering from the neighboring parts of the beam, thus restoring the Bragg peak as well.[25] PrAM
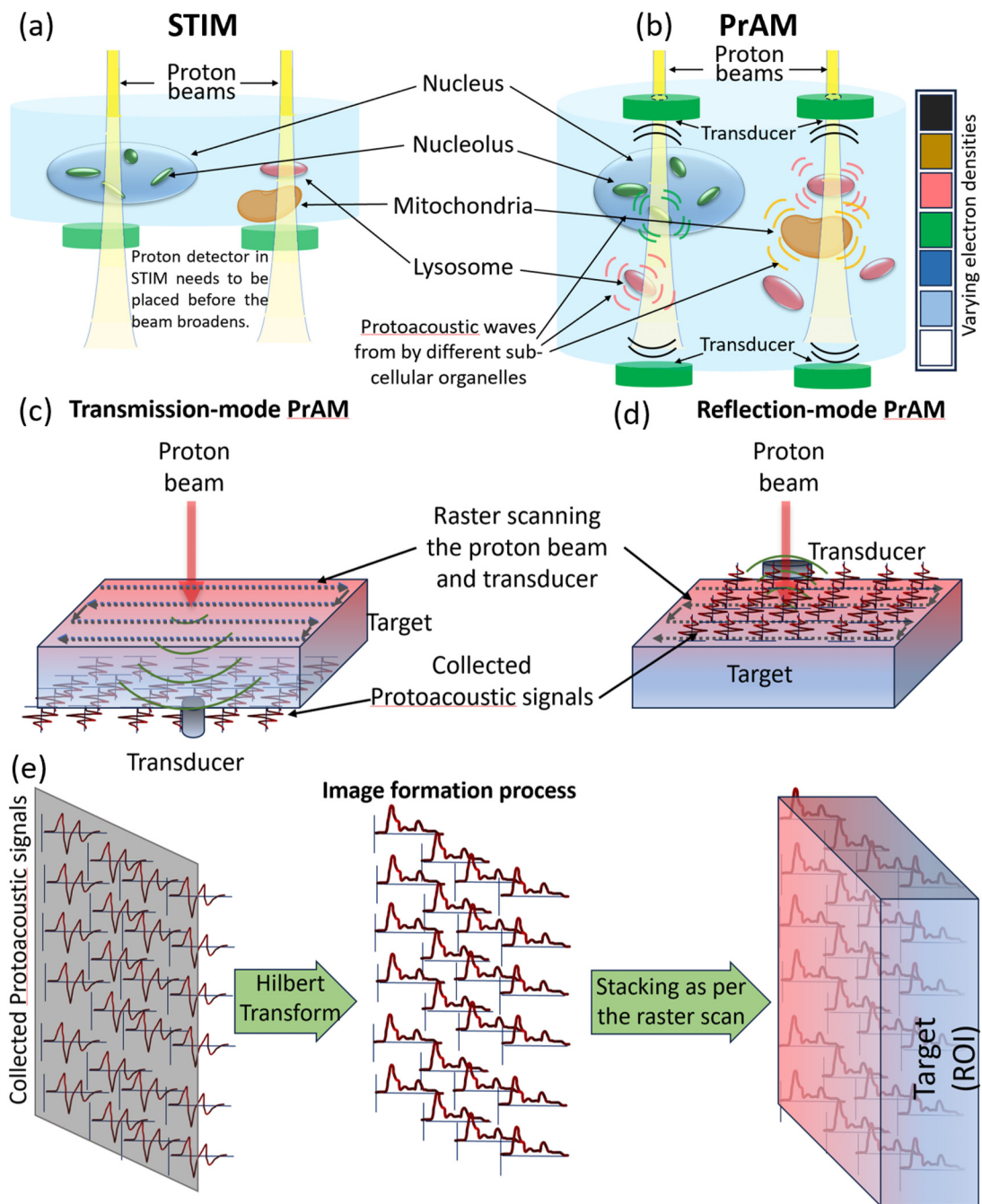
13 February 2024 22:05:43

FIG. 1. Schematic for the underlying principle behind (a) STIM and (b) PrAM. Sketch of the setups for (c) transmission and (d) reflection-mode PrAM, and (e) the process of forming the image from the protoacoustic signals collected via raster scan.

signals are generated from well before the predicted proton range (where BP would be expected for a broad beam). For example, the expected range for 2 MeV protons is $\sim$75 μm.[27] However, the PrAM signals originate from the first $\sim$5 μm, after which the proton energy deposited becomes very small.

When pulsed proton radiation is absorbed by tissues, it triggers the generation of protoacoustic waves resulting from the thermoelastic expansion of the irradiated tissue. These protoacoustic waves have been detected by numerous research groups worldwide[28–32] and are now being employed for on-line range verification and dose

monitoring during the treatment. The propagation of protoacoustic waves in an acoustically homogeneous medium follows the acoustic wave propagation equation,[33]

$$\frac{\partial^2 p(\vec{r}, t)}{\partial t^2} - v^2 \nabla^2 \mathrm{p}(\vec{r}, t) = \Gamma E(\vec{r}) \frac{\partial \mathrm{E}(t)}{\partial t}, \tag{4}$$

where Γ is the Gruneisen parameter, v is the speed of sound in the medium, $\mathrm{E}(\vec{r})$ is the spatial proton energy deposition distribution, and E(t) represents the temporal evolution of the PED. For pulsed proton beams with the pulse width satisfying thermal and stress confinement,[33] E(t) can be reasonably approximated to a Dirac delta function. For such a case, $\mathrm{p}(\vec{r}, t)$ can be understood as the spatiotemporal evolution of a pressure source created by instantaneous proton energy deposition $\mathrm{E}(\vec{r})$ in the medium. The pressure signals collected at the surface of the probed sample have the depth information encoded in the time-domain samples.

Through several *in silico* studies (employing Monte Carlo method for modeling proton energy deposition[34] and k-wave pseudospectral method for modeling acoustic propagation[35]), we demonstrate that PrAM has the capability to facilitate 3D microscopy with sub-50 nm lateral and sub-micron axial resolution from a single raster-scanning of the sample. The transmission and reflection mode PrAM setups are sketched in Figs. 1(c) and 1(d), respectively. The process of forming the image from the collected protoacoustic signals is demonstrated in Fig. 1(e).

For beam scanning-based microscopic applications (STIM and PrAM), thin proton beams are employed. The main factor governing the lateral resolution in STIM and PrAM is the proton beam size, which is affected by beam straggling as the protons penetrate deeper in the sample. In the literature, MeV proton beams are known to be focused to a beam width of ~20 nm using quadruple lenses.[18,20] While the paths of MeV protons remain largely unchanged as they traverse several micrometers in the specimen, slower ions cannot penetrate through a few micrometers thick biological samples. Toward the end of their range, slower ions encounter nuclear scattering, which causes the beam to disperse, consequently diminishing the depth of imaging.

The penetration depth and resolution capability of the MeV proton beams were analyzed via Monte Carlo simulations, which were executed using TOPAS.[34] Simulations were performed to model the proton energy deposition (PED) in water for 1, 2, and 5 MeV protons.

The proton incident direction for each of the simulations was aligned with the positive z-axis, and the beam diameter was chosen to be 10 nm. PED was recorded on X = 0.2 μm × Y = 0.2 μm × Z = 4 μm, 6 μm, and 8 μm grids for 1, 2, and 5 MeV protons, respectively, with 2 nm grid resolution.

Figures 2(a)–2(c) demonstrate the PED maps in the xz-plane for the three energies. The depths at which the PED is less than 10% of the maximum PED is discarded in the analysis, assuming that the protoacoustic signals originating after this distance will have lower SNR. The beam profiles at different depths were fitted to a Gaussian, and the variation of FWHMs with depth is plotted in Figs. 2(d)–2(f) to demonstrate the lateral broadening of the beam. When protons pass through matter, they interact with the atoms and electrons in the material, which causes them to undergo multiple small-angle deflections. As expected, the beam broadens as it penetrates deeper into the tissue. Moreover, the higher energy protons deflect less, and hence, at the same depth, the higher energy beam broadens less in comparison with the lower energy beams. As indicated in Figs. 2(d)–2(f), sub-50 nm resolution can in principle be achieved until up to ~2 μm for 1 MeV protons. For 2 MeV protons, <40 nm resolution is expected until ~4 μm imaging depth, after which the PED becomes lower than the 10% of the maximum PED. Similarly, for 5 MeV protons, <20 nm resolution is expected until ~6 μm imaging depth, after which the PED becomes lower than the 10% of the maximum PED.

These results demonstrate that the kinetic energy of protons can be used as a tuning parameter for improving the imaging depth without compromising the spatial resolution. Along with the imaging depth and resolution, image contrast is another fundamental aspect of microscopy and plays a crucial role in enhancing the visibility and differentiation of objects or structures under observation. It refers to the difference in intensity, color, or other properties between an object of interest and its background or surrounding environment. Protons with kinetic energy of ~2 MeV are known to distinguish among various subcellular organelles with reasonable contrast.[20]

However, with increasing proton energy, this contrast is expected to worsen, and therefore, increasing the proton energy may not always be the best choice. As discussed previously, the axial energy deposition is restored by the in-scattering of protons from around the axis. Therefore, the imaging depth can also be tuned without losing the contrast by simply increasing the beam width. This, however, would affect
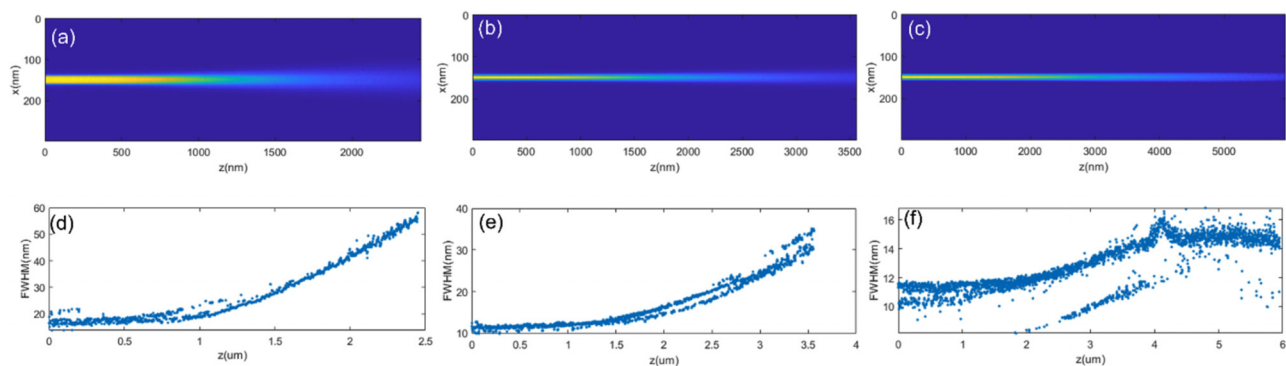

FIG. 2. The PED map in the xz plane and the variation of beam width (FWHM) with depth respectively for [(a) and (d)] 1 MeV, [(b) and (e)] 2 MeV, and [(c) and (f)] 5 MeV proton energies.
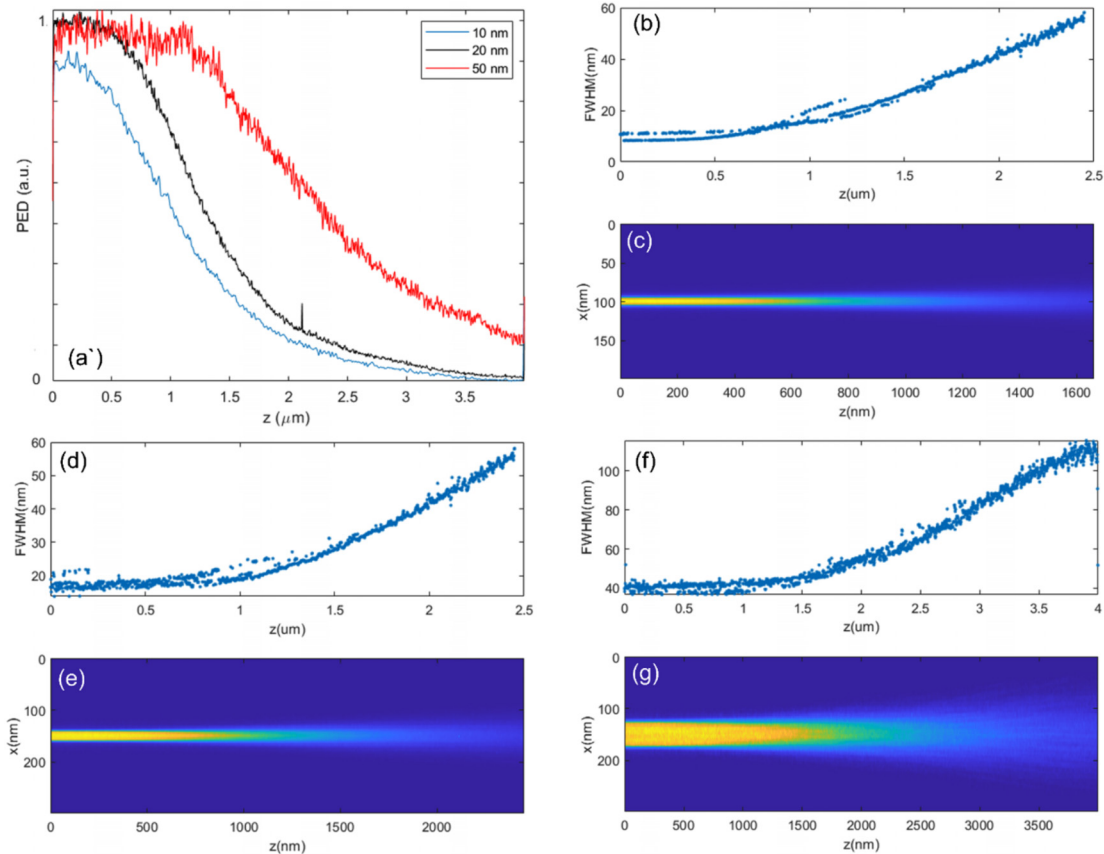
FIG. 3. [1 MeV Proton beam] (a) Variation in the PED characteristics with varying beam size, the FWHM of the PED at different depths, and the PED map in the xz-plane, respectively, for beam diameters [(b) and (c)] 10 nm, [(d) and (e)] 20 nm, and [(f) and (g)] 50 nm.

the lateral spatial resolution of the image. To validate this, we performed TOPAS simulations for 1 MeV proton beams with 10, 20, and 50 nm diameter, and the variation of axial PED with distance for these beam sizes is depicted in Fig. 3(a). As expected, with increased beam size, the axial fluence is restored and the penetration depth increases. However, this comes at the cost of the lateral resolution as shown in Figs. 3(b)–3(g).

Next, we performed a coupled proton-induced acoustic simulation to demonstrate the feasibility of PrAM. For this study, we chose a 1.5 MeV proton beam scanning transmission ion microscopy (STIM) image (size: $40 \times 40 \ \mu m^2$) [Fig. 4(a)] of a HeLa cell pre-dried on a 100-nm thick Si3N4 window.[36] For ease of computation, we only chose a small region around a cell nucleolus as shown in Fig. 4(b). We also added perturbation at a point in the image as indicated in Fig. 4(b), to analyze the resolution capabilities of PrAM. Figure 4(c) shows the slice stacked for protoacoustic simulation for 2 MeV protons at 1, 2, 3, 4, and 5 μm.

As shown in Fig. 5(a), a $100 \times 100 \ nm^2$ cross section was selected as the region of interest and the 3D acoustic propagation was simulated with the limit in the z-direction of the domain set to 5 μm. A point transducer was located at the $x = y = z = 0$. The grid resolution (h) was set to be 2 nm. Such a discretization leads to the maximum
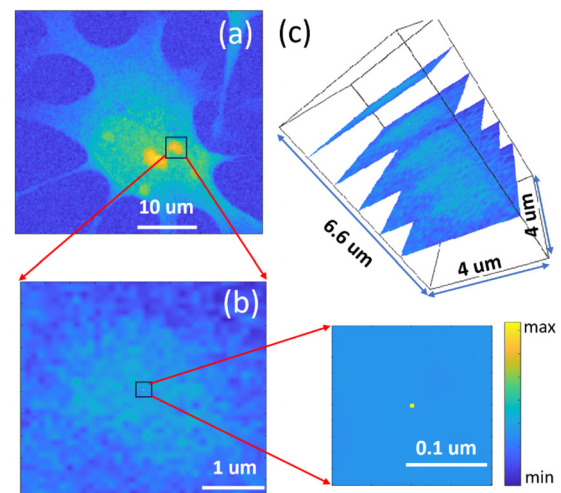

FIG. 4. (a) 1.5 MeV proton STIM image of HeLa cell, (b) the region chosen for simulation in this work, and (c) the slice stacked for protoacoustic simulation for 2 MeV protons at 1, 2, 3, 4, and 5 μm.
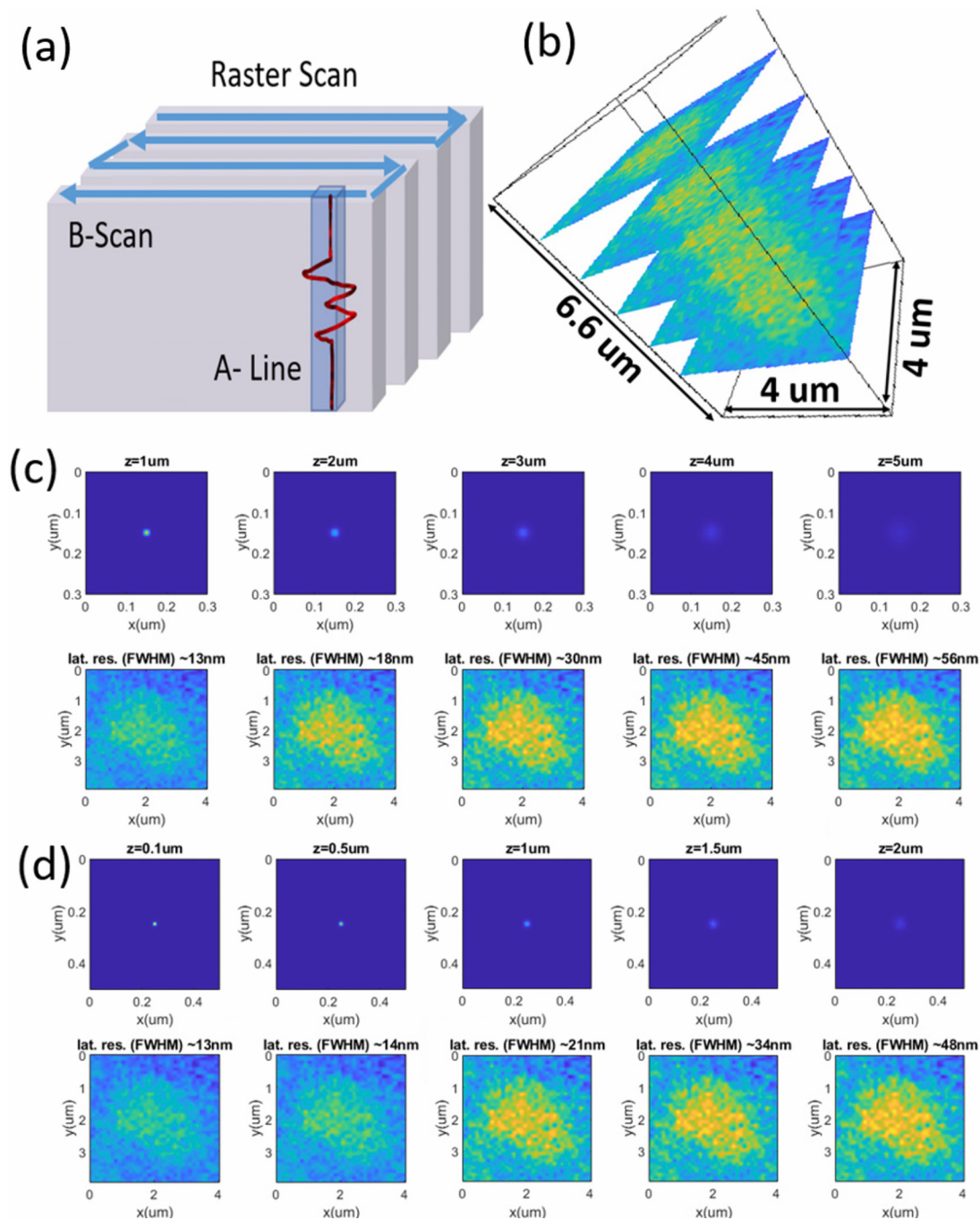
FIG. 5. (a) A sketch demonstrating the raster scanning used for PrAM simulations, (b) the 3D rendering of the PrAM image in the ROI, and (c) first row: 2D PED map at different depths for 2 MeV protons and second row: corresponding PrAM slices and resolutions.

supported frequency of $f_{max} = v/2h = 375$ GHz. The sampling frequency has, therefore, been chosen to be $f_s = 1$ THz, satisfying the Nyquist–Shannon sampling criterion ($f_s > 2f_{max}$).[37] The simulated signals were then contaminated with white Gaussian noise to have 5 dB SNR in the measurements.

This acoustic propagation box was then scanned across the whole region of interest as indicated in Fig. 5(a), in 10 nm steps mimicking the raster scanning of the source and transducer together. The recorded A-scans were then Gaussian filtered and then subsequently Hilbert transformed. Each Hilbert transformed A-scan represents a

single column of data, and when stacked side by side as per the raster-scan, the 3D microscopic image of the complete ROI was formed, as shown in Fig. 5(b) for the 2 MeV protons simulation. To evaluate the lateral spatial resolution of PrAM at different depths, the lateral profile across the perturbed point was fitted to a Gaussian and sub-50 nm lateral resolution (FWHM) was obtained until 2 and 5 μm for 1 MeV [Fig. 5(c)] and 2 MeV [Fig. 5(d)] protons.

Ionic-resolution PrAM employs the lateral scanning of the thin proton beam. Therefore, the lateral resolution of PrAM at any depth is expected to be equal to the beam broadening. The axial resolution (AR), on the other hand, is dependent upon the transducer bandwidth (AR $\sim 0.88\, v_s/\Delta f$; Δf being the transducer's bandwidth[38,39]). Commonly used ultra-high frequency piezoelectric transducers are known to have up to hundreds of MHz (up to 1 GHz) bandwidth[40,41] for sensing the acoustic signals, and one can expect $\sim$1–10 μm axial resolution. However, <200 nm axial resolution can be achieved leveraging pump–probe techniques, which can facilitate >1 GHz frequency bandwidth and are widely employed in picosecond ultrasonics.[8,42] To achieve such axial resolutions, the excitation proton pulse duration (τ) must satisfy the stress confinement, i.e., $\tau <$ AR/v_s. Therefore, to achieve <200 nm axial resolution, the pulse duration should be less than $\sim$0.15 ns. Laser-driven proton beams are known to have the pulse durations of a few picoseconds and hence easily satisfy this criterion.[43–45]

The simulation studies we conducted suggest a high likelihood of experimental realization. For pulsed clinical proton machines ($\sim$100–250 MeV protons and $\sim\mu$s pulse duration), generation and sensing of protoacoustic waves has been reported by several groups across the globe.[28,30,46] Protoacoustic signals generated from $\sim$20 MeV protons with 200 ns pulse duration have also been reported.[47] Laser-driven proton beams are known to have the pulse durations of a few picoseconds[43–45] and are expected to be more suitable for PrAM as they easily satisfy the stress and thermal confinement conditions. MeV protons are known to demonstrate distinguishable contrast between subcellular organelles, and researchers have been able to focus such proton beams to $\sim$20 nm using quadruple lenses. Therefore, proton STIM has been reported to achieve super-resolution imaging of cells.[20] So far in the proton STIM literature,[18,20,21] researchers have reported visualizing cell nucleus, nucleoli, and filopodia, which we expect to see in PrAM as well. Since the contrast mechanism depends on energy deposition of the incident ions, an immediate problem is that visualizing some organelles within the cytoplasm with similar electron density as cytoplasm would be difficult as they may be indistinguishable from the surrounding. More information in this context can only be provided after preliminary PrAM experiments. Protons fluence decreases as they penetrate deeper in the tissue, and hence, the visibility of the deeper structures is expected to worsen in PrAM images. Therefore, development of proton fluence correction techniques will prove to be useful to improve the visualization of the deeper entities via PrAM.

Temperature rise and possible thermal damages for photoacoustic imaging have been assessed in several papers.[48–50] These studies have consistently found that the heat deposition necessary for photoacoustic imaging is generally safe and does not result in cell deaths. Indeed, photoacoustic imaging has demonstrated that a few mK temperature rise in the sample can produce reasonably strong acoustic signal.[33] The proton fluence in the PrAM beam will be chosen accordingly to satisfy this criterion. Moreover, due to the short pulse widths of the proton beams to be used in PrAM, high instantaneous dose rates are expected, which would induce FLASH effect resulting in a significant reduction in radiation toxicity to normal cells.

In this paper, we demonstrated the feasibility of a microscopic imaging technique—protoacoustic microscopy—via *in silico* studies. The results indicate the capability of the proposed modality for three-dimensional imaging of cells with sub-50 nm lateral and $\sim$1 μm axial resolution using traditional ultra-high-frequency piezoelectric transducer as the detector. Employing pump-probe based detection can further improve the axial resolution and can facilitate super-resolution imaging axially as well. The PrAM image represents the proton energy deposition in the target, which is dependent on the chemical composition of the intracellular organelles. Efforts are being made toward the experimental realization of PrAM in collaboration with laboratories with laser-driven proton beamlines.

AUTHOR DECLARATIONS
Conflict of Interest

The authors have no conflicts to disclose.

Author Contributions

Prabodh Kumar Pandey: Conceptualization (equal); Formal analysis (equal); Methodology (equal); Software (equal); Visualization (equal); Writing – original draft (equal); Writing – review & editing (equal). **Gilberto Gonzalez:** Data curation (equal); Software (equal). **Frederick Cheong:** Data curation (equal); Methodology (supporting). **Ce-Belle Chen:** Data curation (supporting); Methodology (supporting); Resources (supporting). **Andrew Anthony Bettiol:** Data curation (equal); Methodology (supporting); Resources (supporting). **Yong Chen:** Funding acquisition (equal); Methodology (equal); Project administration (equal); Resources (equal); Software (equal). **Liangzhong Xiang:** Conceptualization (equal); Funding acquisition (equal); Methodology (equal); Project administration (equal); Supervision (equal); Writing – original draft (equal); Writing – review & editing (equal).

DATA AVAILABILITY

The data that support the findings of this study are available from the corresponding author upon reasonable request.

REFERENCES

[1]Lord Rayleigh, "XXXI. Investigations in optics, with special reference to the spectroscope," London, Edinburgh Dublin Philos. Mag. J. Sci. **8**(49), 261–274 (1879).

[2]M. G. L. Gustafsson, "Surpassing the lateral resolution limit by a factor of two using structured illumination microscopy," J. Microsc. **198**(2), 82–87 (2000).

[3]M. G. L. Gustafsson, L. Shao, P. M. Carlton, C. J. R. Wang, I. N. Golubovskaya, W. Z. Cande, D. A. Agard, and J. W. Sedat, "Three-dimensional resolution doubling in wide-field fluorescence microscopy by structured illumination," Biophys. J. **94**(12), 4957–4970 (2008).

[4]R. Won, "Eyes on super-resolution," Nat. Photonics **3**(7), 368–369 (2009).

[5] B. Park, H. Lee, P. K. Upputuri, M. Pramanik, D. Kim, and C. Kim, "Super-resolution photoacoustic microscopy using near-field localization by a plasmonic metal nanoaperture: A simulation study," IEEE J. Select. Top. Quantum Electron. **25**(2), 4600107 (2019).

[6] X. Song and X. Zhou, Proc. SPIE **11844**, 1184415 (2021).

[7] R. K. Saha and M. C. Kolios, "A simulation study on photoacoustic signals from red blood cells," J. Acoust. Soc. Am. **129**(5), 2935–2943 (2011).

[8] P. Samant, T. A. Burt, Z. J. Zhao, and L. Xiang, "Nanoscale photoacoustic tomography for label-free super-resolution imaging: Simulation study," J. Biomed. Opt. **23**(11), 116501 (2018).

[9] P. K. Upputuri, M. Krisnan, and M. Pramanik, "Microsphere enabled subdiffraction-limited optical-resolution photoacoustic microscopy: A simulation study," J. Biomed. Opt. **22**(4), 045001 (2016).

[10] R. Heintzmann and T. Huser, "Super-resolution structured illumination microscopy," Chem. Rev. **117**(23), 13890–13908 (2017).

[11] D. Cevoli, R. Vitale, W. Vandenberg, S. Hugelier, R. Van Den Eynde, P. Dedecker, and C. Ruckebusch, "Design of experiments for the optimization of SOFI super-resolution microscopy imaging," Biomed. Opt. Express **12**(5), 2617 (2021).

[12] J. Nelson, X. Huang, J. Steinbrener, D. Shapiro, J. Kirz, S. Marchesini, A. M. Neiman, J. J. Turner, and C. Jacobsen, "High-resolution x-ray diffraction microscopy of specifically labeled yeast cells," Proc. Natl. Acad. Sci. U. S. A. **107**(16), 7235–7239 (2010).

[13] M. R. Howells, T. Beetz, H. N. Chapman, C. Cui, J. M. Holton, C. J. Jacobsen, J. Kirz, E. Lima, S. Marchesini, H. Miao, D. Sayre, D. A. Shapiro, J. C. H. Spence, and D. Starodub, "An assessment of the resolution limitation due to radiation-damage in X-ray diffraction microscopy," J. Electron Spectrosc. Relat. Phenom. **170**(1–3), 4–12 (2009).

[14] D. McMullan, "Scanning electron microscopy 1928–1965," Scanning **17**(3), 175–185 (2006).

[15] E. Ruska, *The Early Development of Electron Lenses and Electron Microscopy* (Hirzel, Stuttgart, 1980).

[16] B. J. Inkson, *Materials Characterization Using Nondestructive Evaluation (NDE) Methods* (Elsevier, 2016), pp. 17–43.

[17] C. J. Peddie, C. Genoud, A. Kreshuk, K. Meechan, K. D. Micheva, K. Narayan, C. Pape, R. G. Parton, N. L. Schieber, Y. Schwab, B. Titze, P. Verkade, A. Weigel, and L. M. Collinson, "Volume electron microscopy," Nat. Rev. Methods Primers **2**(1), 51 (2022).

[18] R. Norarat, V. Marjomäki, X. Chen, M. Zhaohong, R. Minqin, C.-B. Chen, A. A. Bettiol, H. J. Whitlow, and F. Watt, "Ion-induced fluorescence imaging of endosomes," Nucl. Instrum. Methods Phys. Res., Sect. B **306**, 113–116 (2013).

[19] M. I. M. Noble, *Electromagnetism, Quanta, and Electron Flow in the Electrophysiology of Living Cells* (World Scientific, 2021).

[20] A. A. Bettiol, Z. Mi, and F. Watt, "High-resolution fast ion microscopy of single whole biological cells," Appl. Phys. Rev. **3**(4), 041102 (2016).

[21] F. Watt, X. Chen, A. B. D. Vera, C. N. B. Udalagama, M. Ren, J. A. V. Kan, and A. A. Bettiol, "The Singapore high resolution single cell imaging facility," Nucl. Instrum. Methods Phys. Res., Sect. B **269**(20), 2168–2174 (2011).

[22] H. W. Lefevre, R. M. S. Schofield, J. C. Overley, and J. D. Macdonald, "Scanning transmission ion microscopy as it complements particle induced x-ray emission microanalysis," Scanning Microsc. **1**(3), 879–889 (1987).

[23] *Radiation Oncology Physics: A Handbook for Teachers and Students*, edited by E. B. Podgoršak and International Atomic Energy Agency (International Atomic Energy Agency, Vienna, 2005).

[24] P. Sigmund, *Particle Penetration and Radiation Effects: General Aspects and Stopping of Swift Point Charges* (Springer, Berlin; New York, 2006).

[25] W. M. Preston and A. M. Koehler, "The effects of scattering on small proton beams," Report No. NASA-CR-84505, 1968.

[26] W. D. Newhauser and R. Zhang, "The physics of proton therapy," Phys. Med. Biol. **60**(8), R155–R209 (2015).

[27] *Proton Therapy Physics*, 2nd ed. edited by H. Paganetti (CRC Press, Boca Raton, FL, 2020).

[28] W. Assmann, S. Kellnberger, S. Reinhardt, S. Lehrack, A. Edlich, P. G. Thirolf, M. Moser, G. Dollinger, M. Omar, V. Ntziachristos, and K. Parodi, "Ionoacoustic characterization of the proton Bragg peak with submillimeter accuracy," Med. Phys. **42**(2), 567–574 (2015).

[29] J. Schauer, H.-P. Wieser, Y. Huang, H. Ruser, J. Lascaud, M. Würl, A. Chmyrov, M. Vidal, J. Herault, V. Ntziachristos, W. Assmann, K. Parodi, and

G. Dollinger, "Proton beam range verification by means of ionoacoustic measurements at clinically relevant doses using a correlation-based evaluation," Front. Oncol. **12**, 925542 (2022).

[30] J. Caron, G. Gonzalez, P. K. Pandey, S. Wang, K. Prather, S. Ahmad, L. Xiang, and Y. Chen, "Single pulse protoacoustic range verification using a clinical synchrocyclotron," Phys. Med. Biol. **68**(4), 045011 (2023).

[31] P. Samant, L. M. Trevisi, Y. Chen, T. Zwart, and L. Xiang, "3-D protoacoustic imaging through a planar ultrasound array: A Simulation workflow," IEEE Trans. Radiat. Plasma Med. Sci. **7**(1), 83–95 (2023).

[32] Y. Nakamura, T. Takayanagi, T. Uesaka, M. B. Unlu, Y. Kuriyama, Y. Ishi, T. Uesugi, M. Kobayashi, N. Kudo, S. Tanaka, K. Umegaki, S. Tomioka, and T. Matsuura, "Technical note: Range verification of pulsed proton beams from fixed-field alternating gradient accelerator by means of time-of-flight measurement of ionoacoustic waves," Med. Phys. **48**(9), 5490–5500 (2021).

[33] L. V. Wang and H. Wu, *Biomedical Optics: Principles and Imaging* (Wiley-Interscience, Hoboken, N.J, 2007).

[34] J. Perl, J. Shin, J. Schümann, B. Faddegon, and H. Paganetti, "TOPAS: An innovative proton Monte Carlo platform for research and clinical applications: TOPAS: An innovative proton Monte Carlo platform," Med. Phys. **39**(11), 6818–6837 (2012).

[35] B. E. Treeby and B. T. Cox, "k-Wave: MATLAB toolbox for the simulation and reconstruction of photoacoustic wave fields," J. Biomed. Opt. **15**(2), 021314 (2010).

[36] R. Minqin, J. A. Van Kan, A. A. Bettiol, L. Daina, C. Y. Gek, B. B. Huat, H. J. Whitlow, T. Osipowicz, and F. Watt, "Nano-imaging of single cells using STIM," Nucl. Instrum. Methods Phys. Res., Sect. B **260**(1), 124–129 (2007).

[37] C. E. Shannon, "Communication in the presence of noise," Proc. IRE **37**(1), 10–21 (1949).

[38] J. Yao and L. V. Wang, "Sensitivity of photoacoustic microscopy," Photoacoustics **2**(2), 87–101 (2014).

[39] L. V. Wang and S. Hu, "Photoacoustic tomography: *In vivo* imaging from organelles to organs," Science **335**(6075), 1458–1462 (2012).

[40] Z. Xie, S.-L. Chen, T. Ling, L. J. Guo, P. L. Carson, and X. Wang, "Pure optical photoacoustic microscopy," Opt. Express **19**(10), 9027 (2011).

[41] M. J. Moore, E. M. Strohm, and M. C. Kolios, "Simultaneous photoacoustic and optical attenuation imaging of single cells using photoacoustic microscopy," in *Proc. SPIE 9708, Photons Plus Ultrasound: Imaging and Sensing* (15 March 2016) edited by A. A. Oraevsky and L. V. Wang (SPIE, San Francisco, California, 2016), p. 970850.

[42] O. Matsuda, M. C. Larciprete, R. Li Voti, and O. B. Wright, "Fundamentals of picosecond laser ultrasonics," Ultrasonics **56**, 3–20 (2015).

[43] H. Daido, M. Nishiuchi, and A. S. Pirozhkov, "Review of laser-driven ion sources and their applications," Rep. Prog. Phys. **75**(5), 056401 (2012).

[44] M. Scisciò, M. Migliorati, L. Palumbo, and P. Antici, "Design and optimization of a compact laser-driven proton beamline," Sci. Rep. **8**(1), 6299 (2018).

[45] J. Bin, J. Obst-Huebl, J.-H. Mao, K. Nakamura, L. D. Geulig, H. Chang, Q. Ji, L. He, J. De Chant, Z. Kober, A. J. Gonsalves, S. Bulanov, S. E. Celniker, C. B. Schroeder, C. G. R. Geddes, E. Esarey, B. A. Simmons, T. Schenkel, E. A. Blakely, S. Steinke, and A. M. Snijders, "A new platform for ultra-high dose rate radiobiological research using the BELLA PW laser proton beamline," Sci. Rep. **12**(1), 1484 (2022).

[46] K. C. Jones, C. M. Seghal, and S. Avery, "How proton pulse characteristics influence protoacoustic determination of proton-beam range: Simulation studies," Phys. Med. Biol. **61**(6), 2213–2242 (2016).

[47] J. Lascaud, P. Dash, M. Würl, H.-P. Wieser, B. Wollant, R. Kalunga, W. Assmann, D.-A. Clevert, A. Ferrari, P. Sala, A. S. Savoia, and K. Parodi, "Enhancement of the ionoacoustic effect through ultrasound and photoacoustic contrast agents," Sci. Rep. **11**(1), 2725 (2021).

[48] T. Sowers, D. VanderLaan, A. Karpiouk, E. M. Donnelly, E. Smith, and S. Emelianov, "Laser threshold and cell damage mechanism for intravascular photoacoustic imaging," Lasers Surg. Med. **51**(5), 466–474 (2019).

[49] E. Newcomer, G. Yang, B. Sun, H. Luo, D. Shen, S. Achilefu, V. Ratts, J. Riley, J. Yeh, and Q. Zhu, "Photoacoustic laser effects in live mouse blastocysts: Pilot safety studies of DNA damage from photoacoustic imaging doses," FS Sci. **1**(1), 53–58 (2020).

[50] P. Samant, J. Chen, and L. Xiang, "Characterization of the temperature rise in a single cell during photoacoustic tomography at the nanoscale," J. Biomed. Opt. **21**(07), 075009 (2016).

13 February 2024 22:05:43